Nano Research
https://doi.org/10.1007/s12274-017-1922-7
Research Article
ISSN 1998-0124
CN 11-5974/O4

Metamaterial-based graphene thermal emitter

Cheng Shi, Nathan H. Mahlmeister, Isaac J. Luxmoore, and Geoffrey R. Nash (✉)

College of Engineering, Mathematics and Physical Sciences, University of Exeter, Exeter, EX4 4QF, UK

Received: 3 July 2017
Revised: 7 November 2017
Accepted: 14 November 2017

KEYWORDS
graphene,
hexagonal boron nitride,
thermal emitter,
infrared,
metamaterial

ABSTRACT

A thermal emitter composed of a frequency-selective surface metamaterial layer and a hexagonal boron nitride-encapsulated graphene filament is demonstrated. The broadband thermal emission of the metamaterial (consisting of ring resonators) was tailored into two discrete bands, and the measured reflection and emission spectra agreed well with the simulation results. The high modulation frequencies that can be obtained in these devices, coupled with their operation in air, confirm their feasibility for use in applications such as gas sensing.

1 Introduction

Many important molecules show their strong characteristic vibrational transitions in the mid-infrared (MIR) spectral region of 2–20 μm [1], which is crucial for applications in spectroscopy [2–4], molecular sensing [5, 6], security [7], imaging [8], etc. However, the development of high-power and efficient MIR sources remains a challenge. Currently there are two main categories of semiconductor MIR sources: bandgap emitters such as MIR light emitting diodes (LEDs), which have high modulation speeds [9] but relatively low radiant power [10]; and MIR cascade lasers. Mid-infrared interband cascade lasers (MIR-ICLs) and quantum cascade lasers (MIR-QCLs) generate photons based on interband transitions and intersubband transitions, respectively, and have demonstrated high output power and efficiency [11, 12]. However, the fabrication of these devices requires the use of precise epitaxial growth, which can lead to additional costs. A less complicated type of MIR source is the incandescent emitter, such as a conventional tungsten filament and a silicon-based micro-machined membrane [13], which has high radiant power. However, due to the low modulation speed and broadband gray-body emission spectrum, these emitters must typically be used in conjunction with choppers and optical filters to achieve a

Address correspondence to g.r.nash@exeter.ac.uk

transient and narrowband emission spectrum for detecting a certain gas or functional group. This adds complexity and cost to the sensor or instrument based on these sources. We have recently explored the potential of multilayered graphene for use as a filament for thermal emitters [14, 15] owing to its superior strength [16], high-temperature stability [17], and extremely high breakdown current density [18]. The low thermal mass and high thermal conductivity [19, 20] enables the graphene emitter to be switched on and off on sub-millisecond timescales [15]. Encapsulation of the graphene with insulating hexagonal boron nitride (h-BN) not only allows for sustained operation in air [14] but also provides a platform for the integration of structures to tailor the emission spectrum.

Previous studies have shown that thermal emission spectra can be engineered using sub-wavelength photonic structures [21–23]. For example, the thermal emission of a tungsten filament in a narrow bandwidth has been enhanced by coupling into the resonant modes of two-dimensional photonic crystals consisting of an array of cylindrical cavities [21, 22]. The advent of metamaterials has also provided a versatile method for manipulating the electromagnetic properties of a device and has been used extensively in designing filters [23], absorbers [24], and super lenses [25], to manipulate the propagation of electromagnetic waves. Following the well-known Kirchhoff's law, the thermal radiation emitted from a device is equal to the radiation that the device absorbs at thermodynamic equilibrium. Based on this, previous studies have verified that metamaterials which act as perfect absorbers on a silicon [26] or tungsten [27] filament can also work as perfect emitters.

In the present study, we have designed, fabricated, and characterized a dual-band emitter based on an encapsulated multilayer graphene. By integrating a planar metamaterial with a boron-nitride encapsulated graphene filament, we demonstrate a thermal emitter with a high modulation speed that can result in a narrow emission bandwidth. This demonstrates the feasibility of fabricating a device with comparable performance to semiconductor LEDs but with better cost-effectiveness and manufacturing sustainability.

2 Design

A dual-band emitter is advantageous for gas-sensing applications, with the wavelength of one emission band being centered at the wavelength of a transparent window, providing a reference, and the other emission band resonant with the absorption of the target gas. Our design, as depicted in Fig. 1(a), consists of three layers: The frequency selective surface (FSS) layer, emission layer, and substrate layer. The metamaterial layer, which tailors the broadband radiation into a dual-band emission, is located at the top surface of the device. For the FSS layer, we used concentric ring resonators, commonly applied in dual-band microwave absorbers, by extending the unit cells to 2 × 2 rings and placing the larger ring resonators diagonally and smaller ring resonators in the off-diagonal direction. The emission layer, i.e., the graphene filament, is connected to gold contacts to allow a bias voltage to be applied. The filament is also encapsulated in a h-BN film to ensure the electrical and thermal isolation of both the metamaterial FSS layer and substrate layer (500 μm-thick highly doped silicon with 300 nm oxide layer), as shown schematically in Fig. 1(a).

Commercial finite difference time domain simulation software, Lumerical Solutions®, was used to analyze the absorption/emission spectrum of the device (see Electronic Supplementary Material (ESM)). The graphene sheet is modelled as a two-dimensional Ohmic layer with conductivity [28, 29]

$$\sigma_{\mathrm{d}} = \frac{ie^2 K_{\mathrm{B}} T}{\pi\hbar^2(\omega + i2\Gamma)}\left[\frac{\mu_{\mathrm{c}}}{K_{\mathrm{B}}T} + 2\ln\left(\mathrm{e}^{-\frac{\mu_{\mathrm{c}}}{K_{\mathrm{B}}T}} + 1\right)\right] + \frac{ie^2}{4\pi\hbar}\ln\left(\frac{2|\mu_{\mathrm{c}}| - (\omega + i2\Gamma)\hbar}{2|\mu_{\mathrm{c}}| + (\omega + i2\Gamma)\hbar}\right) \quad (1)$$

where the two terms on the right-hand side of the equation are the contributions of intraband and interband carrier transitions, respectively (G and m_{c} are the carrier scattering rate and chemical potential within the graphene, respectively). Numerical simulations revealed two peaks in the absorption/emission spectrum, as shown in Fig. 1(b). The calculated electric field distributions, which are plotted in Figs. 1(c) and 1(d), show that the wavelengths of these two emission peaks correspond to the resonant frequencies

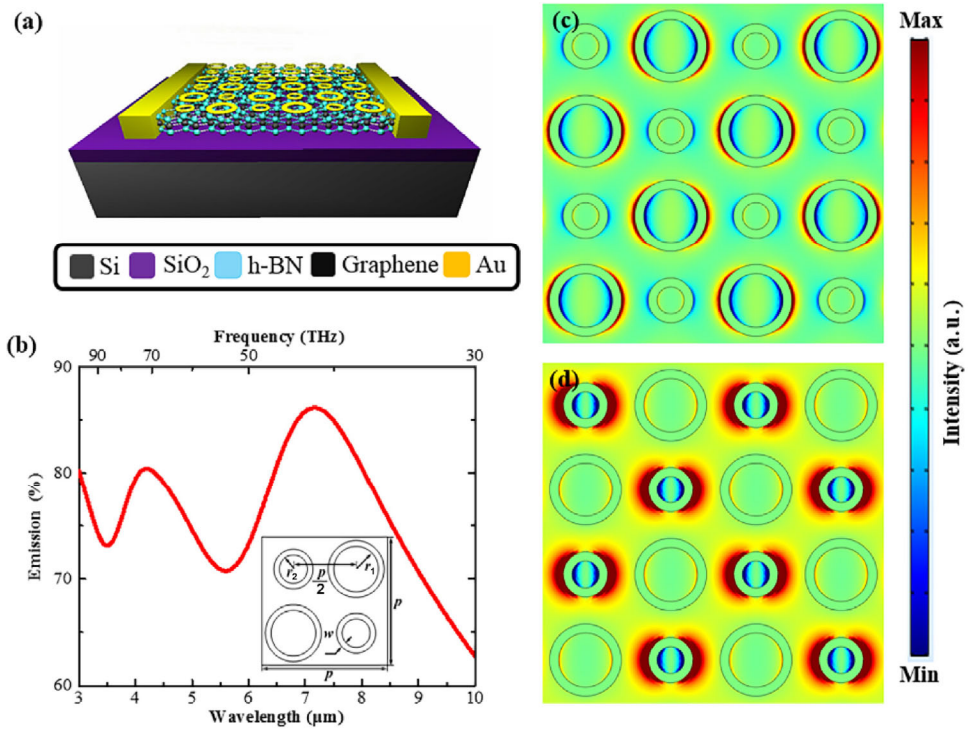

Figure 1 (a) Schematic diagram of the proposed metamaterial graphene mid-infrared emitter. (b) Simulation result of the emission spectrum for the whole device; inset is the definition of the geometrical parameters. (c) and (d) Electric field distributions in the *x*–*y* plane at a wavelength of 4.2 and 7 μm.

of the larger and smaller ring resonators, with the maximum in emission at the high/low frequency corresponding to the small/large ring, respectively. The resonant frequency of a ring resonator can be calculated using Eq. (2) [30]

$$f = \frac{nc}{2\pi r\sqrt{\varepsilon_{\text{eff}}}} \tag{2}$$

where n and c are the mode number and the speed of light in vacuum, r is the average value of the inner radius and outer radius of the ring, and ε_{eff} is the effective permittivity of the metamaterial that can be extracted from the calculated S-parameters. Upon Joule heating, the encapsulated graphene filament radiates energy and the ring resonators resonate in-phase at the resonance frequency, which constructively interferes with the thermal emission from the graphene and enhances the overall radiation. At other frequencies, the overall emission will be reduced because the out-of-phase resonation destructively interferes with the graphene thermal emission. It is clear from Eqs. (1) and (2) that the emission peaks can be located at arbitrary frequencies by changing the geometrical parameters, i.e. the radius of the rings, the periodicity of the unit cell, etc. In this case, we choose r_1 = 200 nm, r_2 = 400 nm, w_1 = w_2 = 200 nm, and p = 3.6 μm to generate two emission peaks at 4.2 μm (f ~ 71 THz) and 7 μm (f ~ 43 THz), which correspond to the CO_2 detection window and a reference window, respectively (Fig. 1(b)).

3 Results and discussion

For a direct comparison between the performance of an emitter with and without metamaterial structure, devices in which the emitting area was divided into four 250 μm × 250 μm quadrants were fabricated, as shown in Fig. 2(a). The two quadrants in the diagonal direction were patterned with ring resonators while the two quadrants in the off-diagonal direction had no ring resonators as a reference. Further details of the fabrication process for the encapsulated graphene emitter can be found in Ref. [19]. Ring resonators, consisting of 5/50 nm-thick Cr/Au, were patterned on the top boron nitride layers of an encapsulated

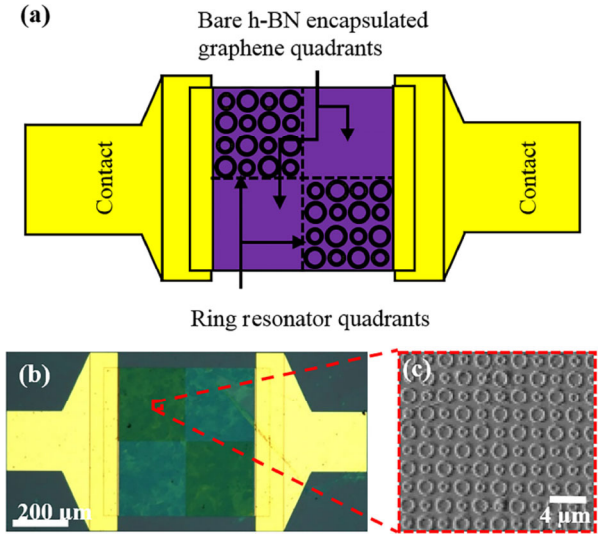

Figure 2 (a) Top view of the schematic illustration of graphene narrowband thermal emitter with quadrants. (b) Microscope image taken at 50× magnification of the top of the emitter. (c) AFM image taken from within the red dash box shown in (b).

multilayer graphene filament (6–8 layers, obtained from ACS Material) using direct-writing electron beam lithography. A 6–8 layered graphene sample was used because it is readily available from suppliers and has a relatively high emissivity [19]. The reflectivity of, and emission from, the devices were characterized using a Fourier-transform infrared (FTIR) Spectrometer. For reflection measurements, light from the FTIR's mid-IR Globar source was focused onto the device using a 40× reflecting objective lens, which was also used to collect the reflected light. The same objective lens was used to collect the emitting thermal radiation when the device was driven by a current. In both the reflection and emission measurements, the spatial variation of the reflection and emission could be measured by scanning the lens, which was mounted on a motorized x–y stage, relative to the device. Further details of the experimental setup are given in the ESM.

Many devices were fabricated and characterized, and the results from one typical device, with the same geometrical parameters used in the simulations, are presented here. Fig. 3(a) shows the measured spatial variation of the total reflection plotted on a logarithmic scale, where the areas with the largest overall measured intensity, the red regions at the top and bottom of the images, are the gold contacts. In

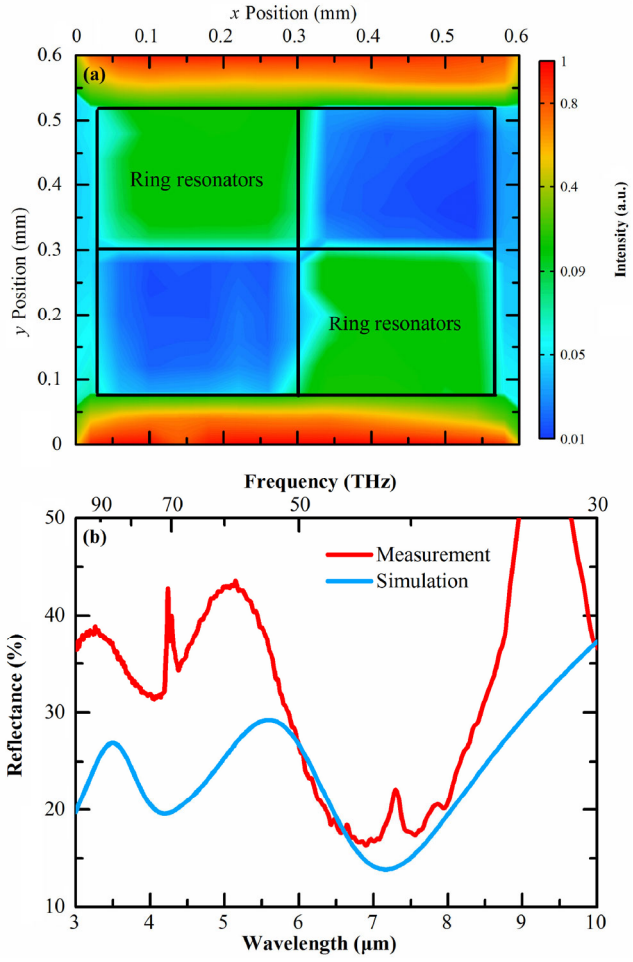

Figure 3 (a) Measured spatial variation of the total reflection intensity on a logarithmic scale. (b) The simulation (blue line) and experimental (red line) spectra for reflection measurements.

the center of the images, two distinct regions are clearly visible pertaining to two groups of quadrants. The two green quadrants on the diagonal direction are those with ring resonators on top of the encapsulated graphene. The two blue quadrants on the off-diagonal direction, with lower measured intensity compared to the green quadrants, correspond to the encapsulated graphene without the ring resonators on top. The increase in the measured reflection intensity from the quadrants with the metamaterial structure is to be expected due to the higher reflectivity of the ring resonator at its non-resonance frequency compared to bare h-BN encapsulated multilayer graphene. The normalized reflection spectrum from the quadrants with ring resonators, as shown in Fig. 3(b), suggests a strong frequency dependence. Two main reflection minima are observed at 4.2 and 7 μm. These two

resonance frequencies, as well as the "W" shaped spectral response, show good agreement with the simulated spectrum. As the measurement was carried out under atmospheric conditions, the sharp peaks at 4.3 and 7.3 μm correspond to CO_2 and water vapor absorption, respectively. The peak in the measured reflectance at 9 μm results from the decrease in transmission through the CaF_2 beam splitter used in the measurement system at wavelengths of 9 μm and higher.

The emission characteristics of the same device were also measured, with the device driven by a 1 kHz square waveform (50% duty cycle), using a Keithley 6221 current source with a peak injection current of 50 mA. The spatial variation of the total thermal emission is plotted on a logarithmic scale in Fig. 4(a). There is a significant difference between the emission

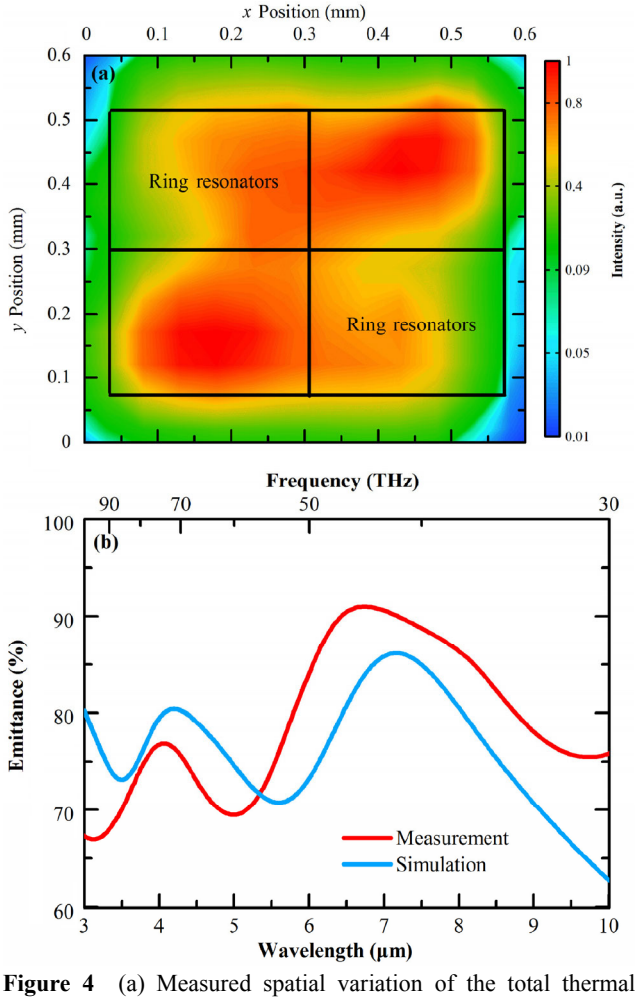

Figure 4 (a) Measured spatial variation of the total thermal emission on a logarithmic scale. (b) The simulation (blue line) and experimental (red line) spectra for emission measurements.

from the quadrants with and without resonators, with higher emission intensity from the quadrants without resonators, consistent with the reflectance measurements. When the emission spectrum from the quadrants with ring resonators is normalized to that from the quadrants without ring resonators, as shown in in Fig. 4(b), a characteristic two-peak spectrum is obtained that is consistent with both the simulated and measured emission and reflection spectra. Numerical simulations also revealed that the performance of the emitter can be dramatically improved by replacing the silicon substrate with more conductive materials. As the dielectric loss in the substrate decreases, the oxide layer becomes a resonant cavity. The increasing conductivity of the substrate will result in an underdamped cavity, which leads to more energy being emitted with a lower decay rate at the resonance frequencies. Besides, the skin depth also dramatically drops along with the increment in the conductivity of the substrate, so that only a relatively thin conducting layer is required. As a result, the amplitude together with the quality factor (Q-factor) of the emission peaks will be substantially increased, as shown in Figs. 5(a) and 5(b), where the calculated emittance is plotted as a function of the substrate conductivity. Using this relatively simple approach, Q-factors of approximately 8.3 can be achieved, which are over two times larger than those of the current commercial MIR-LED sources [9]. The simulated radiation spectrum from the metamaterial graphene thermal emitter with a conducting substrate is shown in Fig. 5(c). The device tailors the gray-body radiation compared to a bare graphene thermal emitter into two main peaks at 6.3 and 4.3 μm. This confirms the feasibility of using this architecture to create an efficient two-channel emitter in which light is emitted at both a gas absorption and reference wavelength.

Finally, the spectral characteristics of the devices can easily be engineered by varying the geometry of the ring resonators. Measurements on other devices with different radii of ring resonators r_1, r_2, and periodicities of the unit cell p also show good agreement with the simulation results (see ESM), highlighting the potential of this device architecture to be used to engineer devices with specific characteristics.

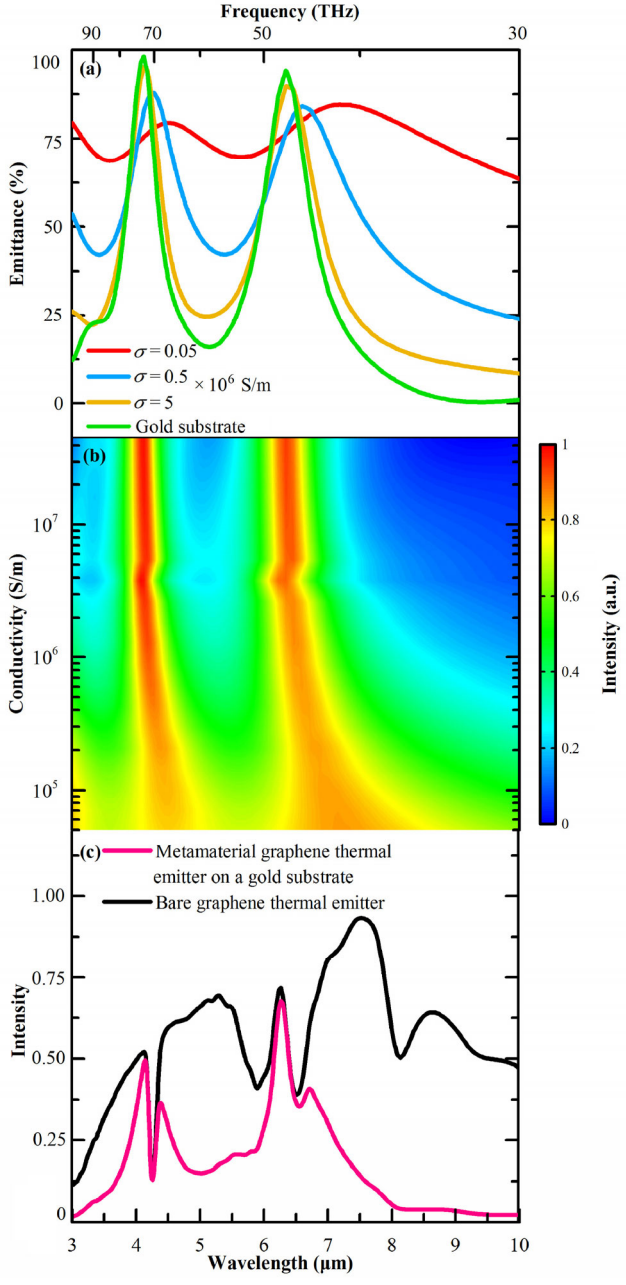

Figure 5 (a) and (b) Emission spectra for substrates with different conductivities. (c) Calculated radiation spectrum of the metamaterial-based graphene thermal emitter on a gold substrate (pink line) based on the measured radiation spectrum of a bare graphene thermal emitter (black line).

4 Conclusions

In conclusion, we have designed, fabricated, and characterized a metamaterial-based encapsulated graphene mid-infrared thermal emitter. The measured reflectance and emission spectra agree well with the simulated results obtained using finite element modeling. At their resonant frequency, the ring resonators enhance the thermal emission from the graphene-based filament, leading to maxima in the emission spectra at wavelengths determined by their geometry. This feature results from the fact that the resonance of the ring resonators at the resonance frequency constructively interferes with the thermal radiation, consequently enhancing the emission energy. Simulations show that the addition of a conducting layer below the emitting layer greatly increases the Q-factor of the maximum in the emission spectrum. The possibility of tailoring the emission characteristics of these devices, which can reduce manufacturing costs and allow for modulation at relatively high frequencies, demonstrates their potential for use in applications such as infrared gas sensing.

Acknowledgements

C.S., I.J.L. and G.R.N. acknowledge financial support from the Engineering and Physical Sciences Research Council (EPSRC) of the United Kingdom via the Centre for Doctoral Training in Electromagnetic Metamaterials (No. EP/L015331/1). G.R.N. also acknowledges the support of EPSRC via a Fellowship in Frontier Manufacturing (No. EP/J018651/1). The authors would like to thank Hannah Barnard for useful discussions.

Electronic Supplementary Material: Supplementary material (FDTD simulation details; measurement setups for both reflection and emission measurements; details of emitters with different geometric parameters and their measurement results) is available in the online version of this article at https://doi.org/10.1007/s12274-017-1922-7.

References

[1] Petersen, C. R.; Møller, U.; Kubat, I.; Zhou, B. B.; Dupont, S.; Ramsay, J.; Benson, T.; Sujecki, S.; Abdel-Moneim, N.; Tang, Z. Q. et al. Mid-infrared supercontinuum covering the 1.4–13.3 μm molecular fingerprint region using ultra-high NA chalcogenide step-index fibre. *Nat. Photonics* **2014**, *8*, 830–834.

[2] Schliesser, A.; Picqué, N.; Hänsch, T. W. Mid-infrared frequency combs. *Nat. Photonics* **2012**, *6*, 440–449.

[3] Stuart, B. H. *Infrared Spectroscopy: Fundamentals and Applications*; Wiley: New York, 2005.

[4] Lee, B. G.; Belkin, M. A.; Audet, R.; MacArthur, J.; Diehl, L.; Pflügl, C.; Capasso, F.; Oakley, D. C.; Chapman, D.; Napoleone, A. et al. Widely tunable single-mode quantum cascade laser source for mid-infrared spectroscopy. *Appl. Phys. Lett.* **2007**, *91*, 231101.

[5] Lin, P. T.; Kwok, S. W.; Lin, H. Y. G.; Singh, V.; Kimerling, L. C.; Whitesides, G. M.; Agarwal, A. Mid-infrared spectrometer using opto-nanofluidic slot-waveguide for label-free on-chip chemical sensing. *Nano Lett.* **2014**, *14*, 231–238.

[6] Wysocki, G.; Weidmann, D. Molecular dispersion spectroscopy for chemical sensing using chirped mid-infrared quantum cascade laser. *Opt. Express* **2010**, *18*, 26123–26140.

[7] Willer, U.; Saraji, M.; Khorsandi, A.; Geiser, P.; Schade, W. Near- and mid-infrared laser monitoring of industrial processes, environment and security applications. *Opt. Lasers Eng.* **2006**, *44*, 699–710.

[8] Soifer, B. T.; Neugebauer, G.; Matthews, K.; Egami, E.; Becklin, E. E.; Weinberger, A. J.; Ressler, M.; Werner, M. W.; Evans, A. S.; Scoville, N. Z. et al. High resolution mid-infrared imaging of ultraluminous infrared galaxies. *Astron. J.* **2000**, *119*, 509–523.

[9] Nash, G. R.; Forman, H. L.; Smith, S. J.; Robinson, P. B.; Buckle L.; Coomber, S. D.; Emeny, M. T.; Gordon, N. T.; Ashley T. Mid-infrared $Al_xIn_{1-x}Sb$ light-emitting diodes and photodiodes for hydrocarbon sensing. *IEEE Sens. J.* **2009**, *9*, 1240–1243.

[10] Haigh, M. K.; Nash, G. R.; Smith, S. J.; Buckle L.; Emeny, M. T.; Ashley T. Mid-infrared $Al_xIn_{1-x}Sb$ light-emitting diodes. *Appl. Phys. Lett.* **2007**, *90*, 231116.

[11] Kim, M.; Canedy, C. L.; Bewley, W. W.; Kim, C. S.; Lindle, J. R.; Abell, J.; Vurgaftman I.; Meyer, J. R. Interband cascade laser emitting at λ = 3.75 μm in continuous wave above room temperature. *Appl. Phys. Lett.* **2008**, *92*, 191110.

[12] Yao, Y.; Hoffman, A. J.; Gmachl, C. F. Mid-infrared quantum cascade lasers. *Nat. Photonics* **2012**, *6*, 432–439.

[13] Ali, S. Z.; De Luca, A.; Hopper, R.; Boual, S.; Gardner, J.; Udrea, F. A low-power, low-cost infra-red emitter in CMOS technology. *IEEE Sens. J.* **2015**, *15*, 6775–6782.

[14] Barnard, H. R.; Zossimova, E.; Mahlmeister, N. H.; Lawton, L. M.; Luxmoore, I. J.; Nash, G. R. Boron nitride encapsulated Graphene infrared emitters. *Appl. Phys. Lett.* **2016**, *108*, 131110.

[15] Mahlmeister, N. H.; Lawton, L. M.; Luxmoore, I. J.; Nash, G. R. Modulation characteristics of graphene-based thermal emitters. *Appl. Phys. Express* **2016**, *9*, 012105.

[16] Lee, C.; Wei, X.; Kysar, J. W.; Hone, J. Measurement of the elastic properties and intrinsic strength of monolayer graphene. *Science* **2008**, *321*, 385–388.

[17] Campos-Delgado, J.; Kim, Y. A.; Hayashi, T.; Morelos-Gómez, A.; Hofmann, M.; Muramatsu, H.; Endo, M.; Terrones, H.; Shullf R. D.; Dresselhaus M. S. et al. Thermal stability studies of CVD-grown graphene nanoribbons: Defect annealing and loop formation. *Chem. Phys. Lett.* **2009**, *469*, 177–182.

[18] Murali, R.; Yang, Y. X.; Brenner, K.; Beck, T.; Meindl, J. D. Breakdown current density of graphene nanoribbons. *Appl. Phys. Lett.* **2009**, *94*, 243114.

[19] Basile, G.; Bernardin, C.; Olla, S. Momentum conserving model with anomalous thermal conductivity in low dimensional systems. *Phys. Rev. Lett.* **2006**, *96*, 204303.

[20] Lepri, S.; Livi, R.; Politi, A. Thermal conduction in classical low-dimensional lattices. *Phys. Reports* **2003**, *377*, 1–80.

[21] Celanovic, I.; Jovanovic, N.; Kassakian, J. Two-dimensional tungsten photonic crystals as selective thermal emitters. *Appl. Phys. Lett.* **2008**, *92*, 193101.

[22] Pralle, M. U.; Moelders, N.; McNeal, M. P.; Puscasu, I.; Greenwald, A. C.; Daly, J. T.; Johnson, E. A.; George, T.; Choi, D. S.; El-Kady, I. et al. Photonic crystal enhanced narrow-band infrared emitters. *Appl. Phys. Lett.* **2002**, *81*, 4685–4687.

[23] Gu, J. Q.; Singh, R.; Liu, X. J.; Zhang, X. Q.; Ma, Y. F.; Zhang, S.; Maier, S. A.; Tian, Z.; Azad, A. K.; Chen, H. T. et al. Active control of electromagnetically induced transparency analogue in terahertz metamaterials. *Nat. Commun.* **2012**, *3*, 1151.

[24] Landy, N. I.; Sajuyigbe, S.; Mock, J. J.; Smith, D. R.; Padilla, W. J. Perfect metamaterial absorber. *Phys. Rev. Lett.* **2008**, *100*, 207402.

[25] Aydin, K.; Bulu, I.; Ozbay, E. Subwavelength resolution with a negative-index metamaterial superlens. *Appl. Phys. Lett.* **2007**, *90*, 254102.

[26] Liu, X. L.; Tyler, T.; Starr, T.; Starr, A. F.; Jokerst, N. M.; Padilla, W. J. Taming the blackbody with infrared metamaterials as selective thermal emitters. *Phys. Rev. Lett.* **2011**, *107*, 045901.

[27] Argyropoulos, C.; Le, K. Q.; Mattiucci, N.; D'Aguanno, G.; Alu, A. Broadband absorbers and selective emitters based on plasmonic Brewster metasurfaces. *Phys. Rev. B* **2013**, *87*, 205112.

[28] Gusynin, V. P.; Sharapov, S. G.; Carbotte, J. P. Magneto-optical conductivity in graphene. *J. Phys.: Condens. Matter* **2007**, *19*, 026222.

[29] Gusynin, V. P.; Sharapov, S. G.; Carbotte, J. P. Sum rules for the optical and hall conductivity in graphene. *Phys. Rev. B* **2007**, *75*, 165407.

[30] Hsieh, L. H.; Chang, K. Equivalent lumped elements G, L, C, and unloaded Q′s of closed- and open-loop ring resonators. *IEEE Trans. Microw. Theory Techn.* **2002**, *50*, 453–460.